Variational calculation of the lowest exciton states in phosphorene and transition metal dichalcogenides

José Nuno S Gomes[1]**, Carlos Trallero-Giner**[2] **and Mikhail I Vasilevskiy**[1,3,*]

[1] Centro de Física, Universidade do Minho, Campus de Gualtar, Braga 4710-057, Portugal
[2] Facultad de Física, Universidad de La Habana, Vedado 10400, La Habana, Cuba
[3] International Iberian Nanotechnology Laboratory, Av. Mestre José Veiga s/n, Braga 4715-330, Portugal

E-mail: mikhail@fisica.uminho.pt

CrossMark

Abstract

Several transition metal dichalcogenides (TMDs) can be exfoliated to produce nearly two-dimensional (2D) semiconductor layers supporting robust excitons with non-hydrogenic Rydberg series of states. Black phosphorus (BP) can also be layered to create a nearly 2D material with interesting properties including its pronounced in-plane anisotropy that influences, in particular, exciton states making them different from those in other 2D semiconductors. We apply the Rayleigh–Ritz variational method to evaluate the energies and approximate the wavefunctions of the ground and lowest excited states of the exciton in a 2D semiconductor with anisotropic effective masses of electrons and holes. The electron–hole interaction is described by the Rytova–Keldysh potential, which is considered beyond the standard zero-thickness approximation. The exciton binding energies calculated for BP and TMD (molybdenum disulphide and tungsten disulphide) monolayers are compared with previously published data.

(Some figures may appear in colour only in the online journal)

1. Introduction

Since the first demonstration of unusual electronic properties of monolayer graphene [1], two-dimensional materials have become an important field of research worldwide [2]. These materials can be obtained from natural substances by mechanical or electro-chemical methods of exfoliation. Their three-dimensional forms, in most cases, can be found in nature [2] and this has inspired studies of possible applications of the 2D counterparts among which one can find metals, insulators and a variety of semiconductors [3, 4]. Several transition metal dichalcogenides (TMDs) are nearly 2D semi-

conductor layers with remarkable properties among which are the extremely robust excitons whose energy spectra cannot be described by the hydrogen model [5, 6]. The exciton binding energies depend on the environment and vary in the range of approximately 200–900 meV.

Black phosphorous (BP) is an allotropic form of phosphorous, which is thermodynamically stable at normal conditions and composed of an orthorhombic lattice of phosphorous atoms. Alike graphite, it has a layered structure and the atoms within a layer form six-member rings; however, contrary to graphene, not all of these 6 atoms lie in the same plane. The reduction of this material to the nearly 2D form containing one or few monolayers, named phosphorene, can be compared to the reduction of graphite to graphene and also results in new interesting properties [7, 8]. Calculations have

shown that phosphorene is a semiconductor with the band gap considerably wider than in the 3D form and strongly depending on the number of monolayers [4, 9]. It has been possible to isolate few-layer flakes of phosphorene with a modification of the mechanical exfoliation method [10] and the material has promise for opto-electronics owing to the relatively high carrier mobility and the tunable band-gap energy corresponding to the infrared spectral range [4, 11–13]. Particularly interesting are the non-linear optical properties of phosphorene [14–16].

As a direct band gap semiconductor, phosphorene also supports the formation of excitons and, as in other 2D materials, these excitons are expected to be robust because of the reduced screening [6, 17]. The binding energies that have been measured for phosphorene using infrared photoluminescence (PL), PL excitation and absorption spectroscopy range from 0.1 to 0.9 eV for monolayer phosphorene (it depends on the screening effect from the substrate and overlaying material) [8, 17]. It has been found that the increase in the number of layers can be monitored by an increase in the width of the layer where the exciton is present [17]. Arguably the most interesting property of phosphorene is the anisotropy of its crystallographic structure. Unlike graphene, phosphorene has a corrugated honeycomb structure that is ductile along one of the in-plane crystal directions but stiff along the other [7]. It causes, in particular, the anisotropy of carriers' effective masses, which leads to anisotropic transport properties and greatly influences the shape and energies of the excitons and the related optical properties of phosphorene [18].

There is a broad literature on the electronic and exciton properties of TMDs, see references [6, 19] for a recent review. As for the phosphorene, its single-particle electronic band structure has been calculated using the density functional theory (DFT) approaches [7, 9, 11, 20] the tight-binding approximation [21] and the $\boldsymbol{k} \cdot \boldsymbol{p}$ method [18]. Using the Bethe–Salpeter equation on top of the DFT calculations, two-particle (including exciton) properties have been evaluated [9, 11]. However, this approach is computationally very demanding. Alternatively, with input from single-particle calculations and experiments, the Wannier effective mass theory can be used to calculate the exciton energy spectrum assuming confinement of the electron and hole to the material's plane [10]. The precise excitonic states in few-layer BP can be determined by numerical diagonalization of the effective mass Hamiltonian [22]. Yet more attractive, when possible, are semi-analytical approaches, such as the recently proposed perturbation theory approximation where the anisotropy is written in the form of a potential energy term that breaks axial symmetry of an isotropic 2D layer [23].

In the present work, we apply the variational method originally proposed by Ritz [24] to the evaluation of the energies of the ground and lowest excited states of the exciton in a 2D semiconductor with anisotropic electron and hole masses. This approach has been successfully used to find an approximate solution of the Schrödinger equation for reduced-symmetry potentials. For instance, exciton states in very narrow quantum wells were calculated by treating the exciton Bohr radius as a free parameter and minimizing the energy with respect to it for a given well width [25] including the ultimate zero-width

limit [26]. Here we assume the solutions of the Schrödinger equation for the hydrogen-like 2D atom [27] as trial functions and modify them in such a way that they can account for the expected anisotropy. Such a choice looks natural for 2D materials [26]; here we extend it to the lowest-energy excited states. The variational method yield a good approximation to the exact energies of the true eigenstates of the system and also provides an approximate analytical expression for the wavefunction. In the next section, the method is exemplified for a hydrogen-like 2D atom (linked by the Coulomb potential) with an anisotropic reduced mass. To model excitons in 2D semiconductors, we consider the Rytova–Keldysh (RK) potential [28, 29] and its extension to few-monolayer (FML) materials. The results will be presented for (isotropic) FMLs of TMD (MoS_2 and WS_2) and (anisotropic) BP monolayers, free-standing or cladded by boron nitride (h-BN) layers (an h-BN/BP/h-BN structure), including the ground state as the first three excited states (namely, $2s$ and $2p_{x,y}$).

2. Variational method for anisotropic hydrogen-like 2D atom

We will apply the Rayleigh–Ritz variational method to the hydrogen-like 2D atom with an anisotropic reduced effective mass, which is a two-dimensional tensor with the principal components μ_x and μ_y. Choosing the axes along the principal directions of the mass tensor, the relative motion of the two particles is described by the following Hamiltonian:

$$H = \frac{p_x^2}{2\mu_x} + \frac{p_y^2}{2\mu_y} + V_C(r), \qquad (1)$$

where $r = \sqrt{x^2 + y^2}$ is the 2D radius-vector modulus and $V_C(r)$ is the usual Coulomb potential, $V_C(r) = -q^2/r$ with q denoting the absolute value of the electron charge. The Hamiltonian (1) lacks axial symmetry and, to the best of our knowledge, the corresponding Schrödinger equation cannot be solved analytically. However, if we assume $\mu_x = \mu_y$, it does have an analytical solution [27]. In particular, the ground state wave-function has the form

$$\Psi_{10}(r) = \frac{\beta_1}{\sqrt{2\pi}} e^{-\beta_1 \frac{r}{2}}, \qquad (2)$$

with $\beta_1 = 4\mu q^2/\hbar^2$ and the energy $E_1^{(0)} = -2\mu q^4/\hbar^2$.

Considering the anisotropic Hamiltonian (1) with the Coulomb potential, we can assume the following trial function for the ground state:

$$\Psi_1(x, y) = C e^{-\sqrt{ax^2 + by^2}}, \qquad (3)$$

where a and b are some positive parameters ($a, b > 0$) and the constant C is determined by the normalisation condition,

$$C = \sqrt{\frac{2}{\pi}} (ab)^{1/4}. \qquad (4)$$

The ground state energy can be evaluated approximately by requiring an absolute minimum of the function:

$$E(a,b) = \langle \Psi_1 | \hat{H} | \Psi_1 \rangle$$

$$= \left[\frac{\hbar^2}{4} \left(\frac{a}{\mu_x} + \frac{b}{\mu_y} \right) - \frac{q^2}{\pi} \int_0^{2\pi} \right.$$

$$\left. \times \left(\frac{1}{a} + \sin^2 \theta \left(\frac{1}{b} - \frac{1}{a} \right) \right)^{-1/2} \mathrm{d}\theta \right], \quad (5)$$

where the radial integral has been evaluated analytically. Thus, we have two equations from which a and b can be found:

$$\frac{\partial E}{\partial a} = \frac{\partial E}{\partial b} = 0. \quad (6)$$

The integral appearing in (5) can be expressed through the complete elliptic integral $K(1 - b/a)$ [30]. For definiteness, we will assume $\mu_x > \mu_y$ and $a > b$. The system (6) can be rewritten as:

$$U\sqrt{b} - 2\mu_x \frac{b^2}{a^2} K' \left(1 - b/a \right) = 0, \quad (7)$$

$$U\sqrt{b} - \mu_y K \left(1 - b/a \right) + 2\mu_y \frac{b}{a} K' \left(1 - b/a \right) = 0, \quad (8)$$

where $U = \frac{\pi \hbar^2}{8q^2}$ and K' is the derivative of K.

In order to demonstrate the effect of the mass anisotropy, we will assume $\bar{\mu} \equiv \frac{1}{2} \left(\mu_x + \mu_y \right) = m_0$ (m_0 is the free electron mass), and present the results for the energies as a function of $\Delta\mu = \mu_x - \mu_y$. Equations (7) and (8) may be rewritten as:

$$U\sqrt{b} - (2\bar{\mu} + \Delta\mu) \frac{b^2}{a^2} K' \left(1 - b/a \right) = 0; \quad (9)$$

$$(2\bar{\mu} - \Delta\mu) \left(K \left(1 - b/a \right) - 2\frac{b}{a} K' \left(1 - b/a \right) \right)$$

$$- 2 (2\bar{\mu} + \Delta\mu) \left(\frac{b}{a} \right)^2 K' \left(1 - b/a \right) = 0. \quad (10)$$

It is convenient to solve the latter equation for b/a first and then plug the result into equation (9) to obtain b.

The dependence of the binding energy upon $\Delta\mu$ is shown in figure 1 (left panel); E_1 decreases as the mass anisotropy increases since we keep the average mass, $\bar{\mu}$ constant. Also shown is the squared modulus of the wave-function in the origin; this quantity determines the oscillator strength of the exciton transition between the ground state and vacuum, which enters the excitonic susceptibility of the material [31, 32].

$$\chi_{2D} = 2\langle |\mathcal{M}_n(\mathbf{e})|^2 \rangle (E_n - \hbar\omega - \mathrm{i}\hbar\gamma)^{-1}. \quad (11)$$

Here the factor of 2 stands for two spin orientations (or, equivalently, for two valleys), the angular brackets denote averaging over photon polarizations ($\mathbf{e}$), n denotes an exciton state with energy E_n, γ is a broadening parameter, and the matrix element is:

$$\mathcal{M}_n = \langle n | - \hat{\mathbf{d}} \cdot \mathbf{e} | 0 \rangle, \quad (12)$$

where $|0\rangle$ stands for exciton vacuum. In the envelope function approximation, the dipole moment operator $\hat{\mathbf{d}}$ acts only on

the Bloch functions of the conduction and valence bands and yields a material parameter $\mathbf{d}_{CV} = d_{CV}(\vec{e}_x \pm \mathrm{i}\vec{e}_y)/\sqrt{2}$, while

$$|0\rangle = \delta(\vec{r}_e - \vec{r}_h); \qquad |n\rangle = \Psi_n(\vec{r}_e - \vec{r}_h)$$

with $\vec{r}_e$ ($\vec{r}_h$) denoting the electron (hole) radius-vector. Indeed, $|\mathcal{M}_n|^2 \propto |\Psi_n(0)|^2$, which is presented in the left panel of figure 1.

We may also consider some excited states. For this, we need to construct orthogonal trial wave-functions that would resemble the (known) true wave-functions in the isotropic limit. In the latter case, for a given principal quantum number n, there are degenerate states with angular momenta $|l| = 0, \ldots, n - 1$. For instance, for $n = 2$, there are two independent wave-functions; their expressions can be found in reference [27] and they suggest the following form of three trial functions that we need in the anisotropic case:

$$\Psi_{20} = C_{20} (1 - \mathrm{d}\rho_2) \mathrm{e}^{-\rho_2}, \quad \rho_2 = \sqrt{a_{20}x^2 + b_{20}y^2}; \quad (13)$$

$$\Psi_{2x} = C_{2x} x \mathrm{e}^{-\rho_{2x}}, \quad \rho_{2x} = \sqrt{a_{2x}x^2 + b_{2x}y^2}; \quad (14)$$

and

$$\Psi_{2y} = C_{2y} y \mathrm{e}^{-\rho_{2y}}, \quad \rho_{2y} = \sqrt{a_{2y}x^2 + b_{2y}y^2}. \quad (15)$$

These functions are chosen orthogonal to each other. They also must be orthogonal to Ψ_1, which we now rewrite as

$$\Psi_1(x,y) = \sqrt{\frac{2}{\pi}}(a_1 b_1)^{1/4} \mathrm{e}^{-\rho_1}, \quad \rho_1 = \sqrt{a_1 x^2 + b_1 y^2}. \quad (16)$$

The functions Ψ_{2x} and Ψ_{2y} are clearly orthogonal to the s functions and to each other by parity. The orthogonality condition for Ψ_{20} and Ψ_1,

$$\int \Psi_{20} \Psi_1 \, \mathrm{d}x \, \mathrm{d}y = 0, \quad (17)$$

requires a particular choice of the parameter d and equation (17) therefore represents an equation to determine it.

Therefore, evaluation of the state energies E_{2x} and E_{2y} requires finding two parameters for each of them, a_{2x} (a_{2y}) and b_{2x} (b_{2y}). For the $2s$ state, with the energy E_{20}, a_{20} and b_{20} have to be determined and d depends on these two parameters and the previously calculated a_1 and b_1. In the next section, we shall apply this procedure to the Hamiltonian with the RK potential.

3. Results and discussion

3.1. The Rytova–Keldysh potential

The potential felt by a point charge in a thin film is affected by the other charges in the film, as well as by the difference of dielectric functions of the film and the exterior [28]. The Poisson equation for this scenario, in the zero-thickness limit, has the commonly used RK potential as a solution [28, 29]. The electrostatic potential energy for a film of infinitesimal
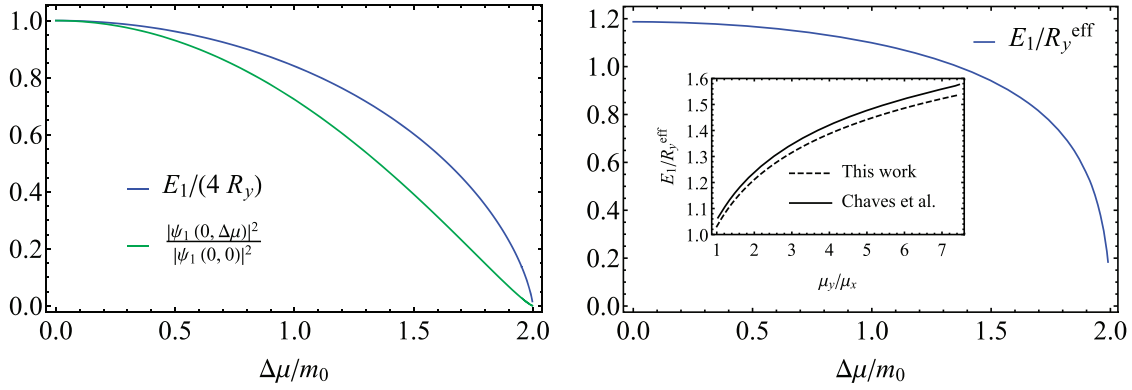
Figure 1. (Left) Ground state energy (blue curve) calculated for Coulomb potential (equations (9) and (10)) plotted as a function of $\Delta\mu$ (in units of m_0, for a fixed $\bar{\mu} = m_0$. The energy values are normalized by the ground state energy for the isotropic case. The green curve shows the relative oscillator strength associated with the excitonic transition, given by the envelope wave-function at $r = 0$. (Right) The same for the RK potential. The parameters are $r_0 = 2.5$ nm and $\kappa = 4.5$, which corresponds to hBN-BP-hBN. The energy is scaled to the effective Rydberg energy, $R_y^{\text{eff}} = R_y \mu_x / (\epsilon_1 + \epsilon_2) m_0$. The inset presents the comparison to the results of figure 4(a) of reference [22] where the energy is plotted against μ_y / μ_x and the parameters used correspond to the system vacuum-BP-SiO$_2$.

thickness, $L \approx 0$, is usually written in the form:

$$V(r) = -\frac{q^2}{r_0}\frac{\pi}{2}\left[H_0\left(\frac{\kappa r}{r_0}\right) - Y_0\left(\frac{\kappa r}{r_0}\right)\right] \equiv -\frac{\pi q^2}{2r_0}\mathcal{K}\left(\frac{\kappa r}{r_0}\right),$$
(18)

where r_0 is the screening length, $\kappa = \frac{\epsilon_1 + \epsilon_1'}{2}$ is the average of the dielectric constants above and below the 2D material, H_0 is the zero-order Struve function and Y_0 the zero-order Neumann function [30]. The Schrödinger equation (1) with the potential (18) describes envelope wave-functions in the effective mass approximation.

Before proceeding to the results of its application to an anisotropic 2D material, which is our main goal, we would like to discuss an extension of equation (18) to a FML 2D semiconductor. As shown in appendix A by using the same approach as the original work [28], the lowest-order finite-thickness correction is given by:

$$\delta V(r) \simeq \frac{-q^2}{\epsilon_2}\left[\frac{\tilde{A}}{r} + \tilde{B}F(\beta, r) + \tilde{C}F\left(\frac{1 - \alpha\beta}{\alpha}, r\right)\right],$$
(19)

where ϵ_2 is the dielectric constant of the film material,

$$\tilde{A} = \frac{1}{\epsilon - 1}, \qquad \tilde{B} = -\frac{2}{\epsilon - 2}, \qquad \tilde{C} = \frac{\epsilon^2 - 2\epsilon + 2}{\epsilon^2 - 3\epsilon + 2}$$
(20)

with $\epsilon = \epsilon_2 / \epsilon_1$ and α, β and $F(\xi, r)$ defined in appendix A.

Before applying equation (19), it is necessary to remind that the physical meaning of the screening parameter r_0 is the static 2D susceptibility of the *monolayer* material (times 2π) [33]. Therefore, we can assume that it is proportional to the number of monolayers (N) in FML films [34],

$$r_{0N} = \tilde{r}_0 N,$$
(21)

where $\tilde{r}_0$ is a fitting parameter. Also, we use $L = l_0 N$ for $n \geqslant 1$. For hypothetical sub-monolayer films ($L < l_0$, the thickness of the WS$_2$ monolayer is $l_0 \approx 1.22$ nm [35]) we take the screening parameter equal to r_0, i.e. $r_{N\leqslant 1} = r_0$.

The potential energy is then expressed as

$$V^{(N)}(r) \simeq \frac{-q^2}{\epsilon_2}\left[\frac{\pi\epsilon_2}{2r_{0N}}\mathcal{K}_0\left(\frac{\kappa r}{r_{0N}}\right) + \frac{\tilde{A}}{r} + \tilde{B}F\left(\frac{\kappa}{r_{0N}}, r\right)\right.$$
$$\left. + \tilde{C}F\left(\frac{\epsilon_2 - \kappa}{r_{0N}}, r\right)\right].$$
(22)

It is plotted in figure 2 (the parameters used are listed in table 1). The correction with respect to the limiting case $L = 0$ exists already in the case of monolayer (where $r_{01} = \tilde{r}_0$). With the increase of N the dependence (22) becomes closer to $1/(\epsilon_2 r)$ (figure 2).

The isotropic ground state energy for N-layer is determined by minimizing the function

$$E_1^{(N)}(a) = \frac{\hbar^2}{2}\frac{a}{\mu} + 4a\int_0^\infty V^{(N)}(r)e^{-2\sqrt{a}r}\,r\,dr,$$
(23)

and the energy of the first excited state ($2s$) is given by

$$E_{2s}^{(N)}(a) = \frac{\hbar^2}{2}\frac{a}{\mu} + \frac{4}{3}a\int_0^\infty V^{(N)}(r)e^{-2\sqrt{a}r}\left(1 - 2\sqrt{a}r\right)^2 r\,dr.$$
(24)

(with a different value of a obtained by the minimization of (24)). The energy of the $2p$ excited state is given by:

$$E_{2p}^{(N)}(a) = \frac{\hbar^2}{2}\frac{a}{\mu} + \frac{8a^2}{3}\int_0^\infty V^{(N)}(r)e^{-2\sqrt{a}r}r^3\,dr.$$
(25)

The energies computed for WS$_2$ assuming infinitesimal thickness ($L = 0$, with the standard RK potential and the 'standard' value of the screening parameter, $r_0 = 7.5$ nm) and for the cases of 1–5 MLs (using the thickness-corrected potential and the adjusted value of the screening parameter, equation (21)) are shown in the right panel of figure 2. They are in a very good agreement with the experimental data [36], as can be seen from table 2.
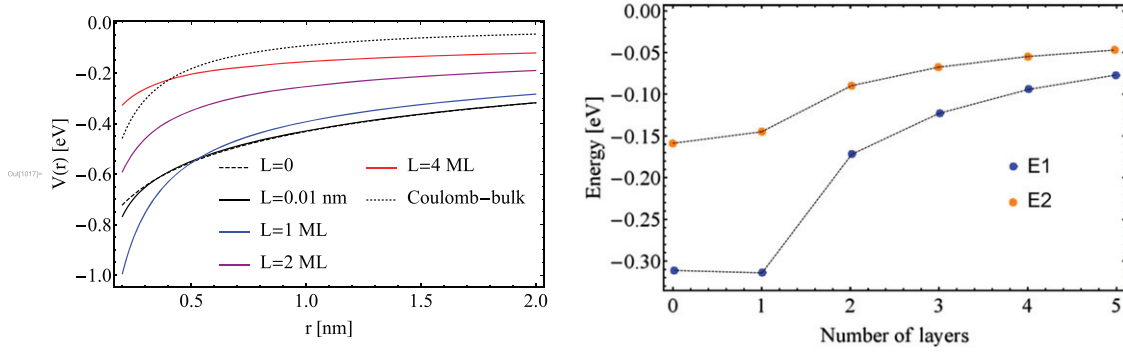
Figure 2. (Left) RK potential for $L = 0$ (dashed curve) and with finite thickness correction for different values of L as indicated ($\kappa = 1$, $l_0 = 1.22$ nm and $r_0 = 7.5$ nm for $L = 0$ and $L = 0.01$, while $\tilde{r}_0 = 9.6$ nm for $L \geqslant 1$). The value of $\tilde{r}_0$ was adjusted to obtain the same value of the exciton binding energy for the cases $L = 0$ (conventional RK potential (18) with the 'standard' r_0 [36, 37]) and $L = 1$ (corrected potential). Also shown is the Coulomb potential for bulk material with dielectric constant $\epsilon_2 = 9.1$ (dotted curve). (Right) Calculated energies of two lowest exciton states in free-standing FML WS$_2$, for different values of L as indicated (the lines are guides to the eye).

Table 1. Parameters used in the calculations.

Parameter	WS$_2$	MoS$_2$	BP
r_0 (nm)	7.5	3.4	2.5
μ (m$_0$)	0.16	0.275	$\mu_x = 0.99$, $\mu_y = 0.12$

Table 2. Comparison of the calculated binding energies (in eV) of the $1s$ and $2s$ states for free-standing WS$_2$ with the results of reference [36].

State	Calculated ($L = 0$)	Experiment
$1s$	0.31	0.32 ± 0.04
$2s$	0.13	0.15 ± 0.04

3.2. Ground state for an anisotropic monolayer

We are not aware of experimental data on exciton energies for FML BP with a well-defined number of monolayers, so we shall employ the standard RK potential (18) here. With the trial function (16), which has been used in reference [20], the energy matrix element is:

$$E_1(a_1, b_1) = \frac{\hbar^2}{4}\left(\frac{a_1}{\mu_x} + \frac{b_1}{\mu_y}\right) - \sqrt{a_1 b_1}\frac{q^2}{r_0}$$
$$\times \int_0^{2\pi}\int_0^\infty \mathcal{K}\left(\frac{\kappa r}{r_0}\right) r e^{-2\sqrt{a_1 + (b_1 - a_1)\sin^2\theta}\, r}\, dr\, d\theta,$$
(26)

where $\mathcal{K}(z) \equiv H_0(z) - Y_0(z)$. Minimization of the energy requires the differentiation of the function given by the double integral in the right-hand side of (26). Fortunately, the integral $\int_0^\infty \mathcal{K}(\beta r)\, e^{-\alpha r}\, dr$ has an analytical expression by means of the entries (6.821) and (6.611) of the Gradshtein and Ryzhik's table of integrals [38]. We define:

$$I(\alpha, \beta) = \int_0^\infty \mathcal{K}(\beta r)\, r e^{-\alpha r}\, dr = -\frac{\partial}{\partial\alpha}\int_0^\infty \mathcal{K}(\beta r)\, e^{-\alpha r}\, dr,$$
(27)

(see appendix B for details). Using this auxiliary function, equations for the a_1 and b_1 coefficients can be written as follows:

$$\frac{\hbar^2}{4\mu_x} - \frac{q^2}{2r_0}\frac{b_1}{a_1}\int_0^{2\pi}\left[I(\alpha, \beta) + \frac{4a_1}{\alpha}\cos^2\theta\frac{\partial I(\alpha, \beta)}{\partial\alpha}\right]d\theta = 0;$$
(28)

$$\frac{\hbar^2}{4\mu_y} - \frac{q^2}{2r_0}\frac{a_1}{b_1}\int_0^{2\pi}\left[I(\alpha, \beta) + \frac{4b_1}{\alpha}\sin^2\theta\frac{\partial I(\alpha, \beta)}{\partial\alpha}\right]d\theta = 0.$$
(29)

The dependence of the binding energy upon the mass anisotropy ($\Delta\mu$ for $\bar{\mu} = \text{const.}$) is shown in figure 1 (right panel). It is qualitatively similar to those for the Coulomb potential (left panel of the same figure), although the absolute values are different. The decrease of the binding energy with $\Delta\mu$ seems to contradict the results presented in figure 4 of reference [22]. Notice, however, that the latter was calculated keeping $\mu_x = \text{const.}$ and varying only μ_y ($\mu_y > \mu_x$ in reference [22]). To avoid confusion, we re-plotted our calculated values against (μ_x/μ_y) keeping $\mu_y = \text{const.}$; this is shown in the inset of figure 1, consistent with the results of reference [22]. The agreement is very good for μ_y close to μ_x and worsens when the anisotropy becomes higher but still is of the order of 3%.

Let us now consider some specific cases characteristic of real materials. For the h-BN/BP/h-BN structure, using the parameters [39] $\kappa = 4.5$ and $r_0 = 2.5$ nm, equations (28) and (29) have the solution $a_1 \approx 2.45$ nm^{-2} and $b_1 \approx 0.533$ nm^{-2}, which yield the energy $E_1^{\text{h-BN/BP/h-BN}} = -257$ meV. For uncovered phosphorene on a SiO$_2$ substrate ($\kappa = 2.4$), a considerably larger (in modulus) value is obtained, $E_1^{\text{BP/SiO}_2} = -454$ meV.

Replacing phosphorene with MoS$_2$ (for which we set $a_1 = b_1$) and using $r_0 = 3.4$ nm and $\mu = 0.275m_0$ (from reference [39]) also yields a shallower ground state with $E_1^{\text{h-BN/MoS}_2/\text{h-BN}} = -215$ meV. Again, it might seem contradicting to what should be expected from figure 1 but remember that we fixed $\frac{1}{2}(\mu_x + \mu_y) = m_0$ in that figure. In reference [39] the value $E_1^{\text{exp}} = -221 \pm 3$ meV was measured for h-BN/MoS$_2$/h-BN. The value obtained here is slightly outside
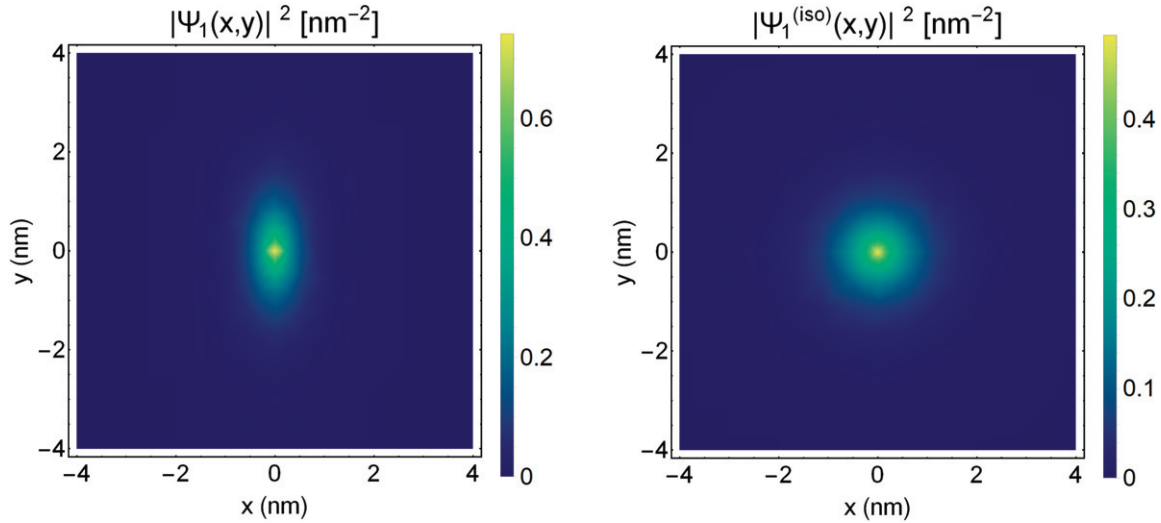
Figure 3. Probability density (in nm^{-2}) distribution for the anisotropic ground state of an h-BN/BP/h-BN structure (left) and for the isotropic ground state of an h-BN/MoS$_2$/h-BN structure (right).

Table 3. Energies (in meV) of the ground and first excited states for different configurations. The values in parentheses are the matrix elements (divided by the elementary charge) for dipole transitions to the ground state.

Materials	BP		MoS$_2$	
State	In h-BN	BP-SiO$_2$	In h-BN	MoS$_2$-SiO$_2$
1s	−257	−454	−215	−367
2s	−56	−135	−49	−114
2p_x	−110 (0.541 nm)	−382	−66 (0.931 nm)	−146
2p_y	−48 (0.271 nm)	−225	−66 (0.931 nm)	−146

of the error bars, but within the interval corresponding to the twice of the indicated standard deviation.

The ground state wave-functions are shown in figure 3. We notice that the wave-function for phosphorene is approximately two times more extended in the y-direction than that for MoS$_2$, while the ground state energies differ by only about 15%. Such a pronounced anisotropy of the envelope wave-function, however, does not directly affect the dipole transition matrix element's dependence upon the polarization of the electric field, **e**, which is determined by the angular dependence of the scalar product $|\mathbf{e} \cdot \mathbf{P}_{cv}|$, where $\mathbf{P}_{cv}$ is the momentum matrix element between the Bloch states of the conduction and valence bands [40]. Yet, the multiplicative factor $|\Psi_1(0)|^2$ depends on the degree of anisotropy and also on the dielectric constants of the cladding layers. We have $|\Psi_1(0)|^2 = 0.729$ nm^{-2} and 0.991 nm^{-2} for phosphorene incorporated into h-BN/BP/h-BN and BP/SiO$_2$ structures, respectively. That is, the transition oscillator strength is considerably higher in the latter case.

3.3. Excited states for an anisotropic monolayer

The normalization constants of the trial wave-functions (13)–(15) are calculated in appendix C. Beginning with the

2p_x state and using the trial wave-function (14), we obtain:

$$E_{2x}(a,b) = \langle \Psi_{2x} | \hat{H} | \Psi_{2x} \rangle = \frac{\hbar^2}{8} \left[\frac{3a}{\mu_x} + \frac{b}{\mu_y} \right]$$

$$+ \frac{8a\sqrt{ab}}{3\pi}$$

$$\times \int_0^\infty \int_0^{2\pi} V(r)\cos^2\theta e^{-2r\sqrt{a+(b-a)\sin^2\theta}} r^3 \, \mathrm{d}r \, \mathrm{d}\theta. \tag{30}$$

Minimization of this energy leads to the equations:

$$\frac{3\hbar^2}{8\mu_x} + \frac{4}{3}\frac{q^2}{r_0}\int_0^{2\pi}\int_0^\infty \left(\frac{r\sqrt{a^3 b}\cos^2\theta}{\sqrt{a+(b-a)\sin^2\theta}} - \frac{3}{2}\sqrt{ab} \right)$$

$$\times \mathcal{K}\left(\frac{\kappa r}{r_0}\right) r^3 \cos^2\theta e^{-2\sqrt{a+(b-a)\sin^2\theta}r} \mathrm{d}r\, \mathrm{d}\theta = 0, \tag{31}$$

$$\frac{\hbar^2}{8\mu_y} + \frac{4}{3}\frac{q^2}{r_0}\int_0^{2\pi}\int_0^\infty \left(\frac{r\sqrt{a^3 b}\sin^2\theta}{\sqrt{a+(b-a)\sin^2\theta}} - \frac{1}{2}\sqrt{\frac{a^3}{b}} \right)$$

$$\times \mathcal{K}\left(\frac{\kappa r}{r_0}\right) r^3 \cos^2\theta\, e^{-2\sqrt{a+(b-a)\sin^2\theta}r} \mathrm{d}r\, \mathrm{d}\theta = 0. \tag{32}$$

The energy can be written in terms of the function $I(\alpha, \beta)$, which is given in appendix B:

$$E_{2x}(a,b) = \langle \Psi_{2x} | \hat{H} | \Psi_{2x} \rangle = \frac{\hbar^2}{8} \left[\frac{3a}{\mu_x} + \frac{b}{\mu_y} \right] + \frac{8\sqrt{a^3 b}}{3\pi}$$

$$\times \int_0^{2\pi} \cos^2\theta \frac{\partial^2}{\partial\alpha^2} I(\alpha, \beta) \mathrm{d}\theta. \tag{33}$$

Solving these equations yields the optimized constants a_{2x} and b_{2x}. For instance, for the h-BN/BP/h-BN structure,
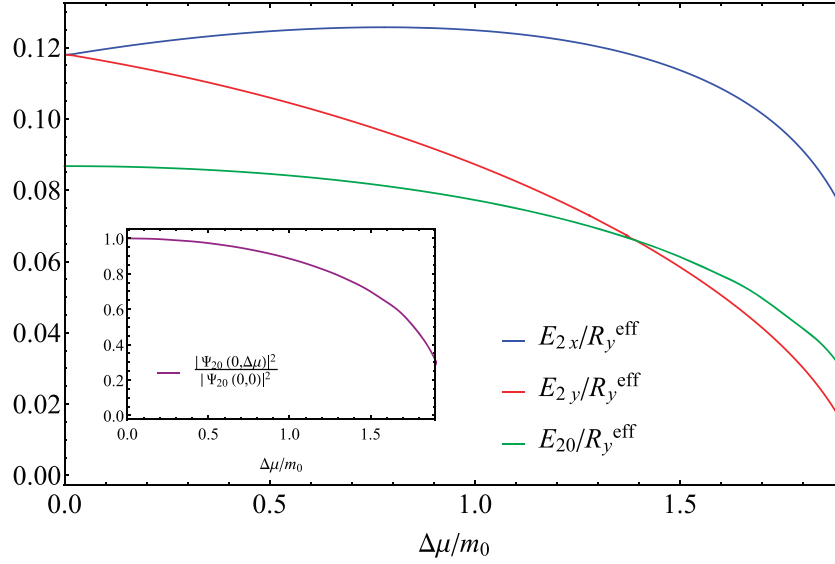
Figure 4. Binding energies of the $2p_x$ (blue), $2p_y$ (red), and $2s$ (green) states plotted as a function of $\Delta\mu$ (in units of m_0), for a fixed $\bar{\mu} = m_0$. The energies are normalized by the corresponding values for the isotropic case (where $\mu_x = \mu_y = m_0$). The inset shows the relative oscillator strength associated with the exciton creation/recombination transition.

Table 4. Dipole moments (divided by the elementary charge) for transitions $|0\rangle \rightarrow |1s\rangle$ and $|0\rangle \rightarrow |2s\rangle$ in nm.

Materials	BP		MoS$_2$	
State	In h-BN	BP-SiO$_2$	In h-BN	MoS$_2$-SiO$_2$
$1s$	0.854	1.067	0.695	0.859
$2s$	0.457	0.644	0.311	0.701

using $\mu_x = 0.9933m_0$ and $\mu_y = 0.12m_0$ [41], we get $a_{2x} \approx 2.30\,\text{nm}^{-2}$ and $b_{2x} \approx 0.610\,\text{nm}^{-2}$, corresponding to the energy $E_{2x}^{\text{h−BN/BP/h−BN}} = -107$ meV.

Similar, for the $2p_y$ state with the trial wave-function (15), we have:

$$E_{2y}(a,b) = \frac{\hbar^2}{8}\left[\frac{a}{\mu_x} + \frac{3b}{\mu_y}\right] + \frac{8\sqrt{ab^3}}{3\pi}$$
$$\times \int_0^\infty \int_0^{2\pi} V(r)r^2\sin^2\theta e^{-2r\sqrt{a+(b-a)\sin^2\theta}}\,r\,\mathrm{d}r\,\mathrm{d}\theta$$

(34)

and the equations for a and b,

$$\frac{\hbar^2}{8\mu_x} + \frac{4}{3}\frac{q^2}{r_0}\int_0^{2\pi}\int_0^\infty \left(\frac{r\sqrt{ab^3}\cos^2\theta}{\sqrt{a+(b-a)\sin^2\theta}} - \frac{1}{2}\sqrt{\frac{b^3}{a}}\right)$$
$$\times \mathcal{K}\left(\frac{\kappa r}{r_0}\right)r^3\sin^2\theta e^{-2\sqrt{a+(b-a)\sin^2\theta}r}\,\mathrm{d}r\,\mathrm{d}\theta = 0;$$

(35)

$$\frac{3\hbar^2}{8\mu_y} + \frac{4}{3}\frac{q^2}{r_0}\int_0^{2\pi}\int_0^\infty \left(\frac{r\sqrt{ab^3}\sin^2\theta}{\sqrt{a+(b-a)\sin^2\theta}} - \frac{3}{2}\sqrt{ab}\right)$$
$$\times \mathcal{K}\left(\frac{\kappa r}{r_0}\right)r^3\sin^2\theta e^{-2\sqrt{a+(b-a)\sin^2\theta}r}\,\mathrm{d}r\,\mathrm{d}\theta = 0.$$

(36)

Again, the energy can be written in terms of the function $I(\alpha, \beta)$ (appendix B):

$$E_{2y}(a,b) = \langle\Psi_{2y}|\hat{H}|\Psi_{2y}\rangle = \frac{\hbar^2}{8}\left[\frac{a}{\mu_x} + \frac{3b}{\mu_y}\right] + \frac{8\sqrt{ab^3}}{3\pi}$$
$$\times \int_0^{2\pi}\sin^2\theta\frac{\partial^2}{\partial\alpha^2}I(\alpha,\beta)\mathrm{d}\theta.$$

(37)

Numerical solution of (35) and (36) yields the optimal values of a_{2y} and b_{2y}. The calculated values of E_{2y} for the h-BN/BP/h-BN structure are given in table 3.

Finally, the total energy for the Ψ_{20} state is:

$$E_{20}(a,b) = \langle\Psi_{20}|\hat{H}|\Psi_{20}\rangle = \frac{\hbar^2}{4}\left(\frac{a}{\mu_x} + \frac{b}{\mu_y}\right)\frac{2+d^2}{2-4d+3d^2}$$
$$- \frac{q^2}{r_0}\frac{2\sqrt{ab}}{2-4d+3d^2}\times\int_0^\infty\int_0^{2\pi}\mathcal{K}\left(\frac{\kappa r}{r_0}\right)$$
$$\times (1 - d\sqrt{a+(b-a)\sin^2\theta}r)^2\,re^{-2\sqrt{a+(b-a)\sin^2\theta}r}\,\mathrm{d}r\,\mathrm{d}\theta,$$

(38)

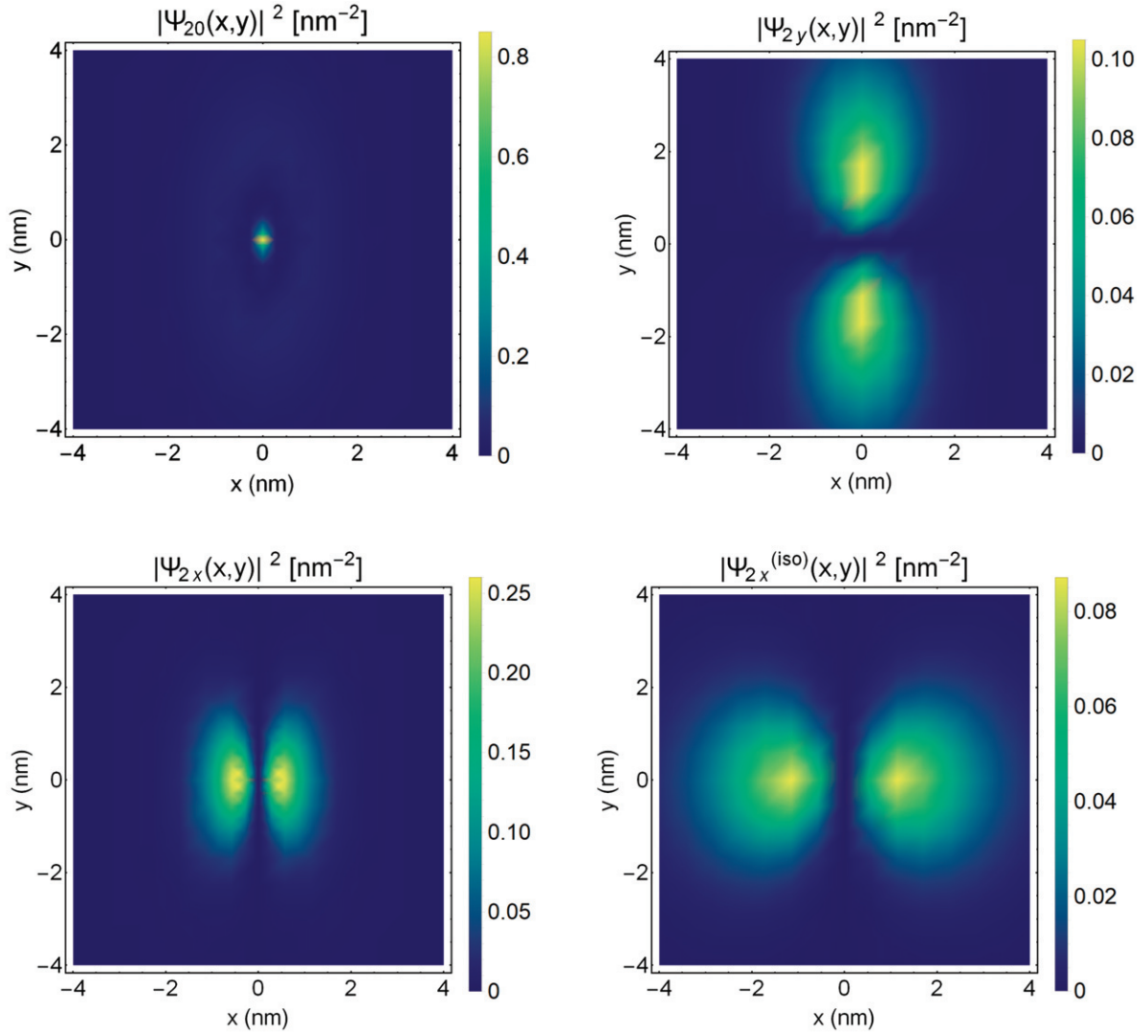or, written in terms of the function $I(\alpha, \beta)$,

Figure 5. Probability density (in nm^{-2}) distribution for the lowest excited states in the h-BN/BP/h-BN structure: $2s$ (top left), $2p_y$ (top right) and $2p_x$ state (bottom left). For comparison, also shown is the $2p_x$ state in the (isotropic) h-BN/MoS$_2$/h-BN structure (bottom right).

$$E_{20}(a,b) = \langle \Psi_{2x} | \hat{H} | \Psi_{20} \rangle$$

$$= \frac{1}{2 - 4d + 3d^2} \left[\frac{\hbar^2}{4} \left(\frac{a}{\mu_x} + \frac{b}{\mu_y} \right) (2 + d^2) \right.$$

$$\left. \qquad (39)$$

$$\left. - 2\sqrt{ab} \frac{q^2}{r_0} \int_0^{2\pi} \left(1 + \alpha \frac{d}{2} \partial_\alpha \right)^2 I(\alpha, \beta) \mathrm{d}\theta \right].$$

$$(40)$$

The condition of orthogonality that determines d (17) yields:

$$\int_{-\infty}^{\infty} \int_{-\infty}^{\infty} \left(1 - \sqrt{ax^2 + by^2} d \right) e^{-\sqrt{a_1 x^2 + b_1 y^2}} e^{-\sqrt{ax^2 + by^2}} \, \mathrm{d}x \, \mathrm{d}y = 0,$$

$$(41)$$

where a_1 and b_1 are the optimized constants for the state Ψ_1. Therefore, this parameter must be treated as a function of a and b, $d = d(a,b)$, when solving equations $\partial_a E_{20}(a,b) = 0$ and $\partial_b E_{20}(a,b) = 0$. The technical procedure that facilitates solution of this system of equations is presented in appendix D and the conditions (D.8) determine the solution. For instance, for the h-BN/BP/h-BN structure we obtain: $a \approx 0.72$ nm^{-2}, $b \approx 0.14$ nm^{-2}, $d \approx 1.397$ and $E_{20}^{\text{h-BN/BP/h-BN}} = -56$ meV.

The energies of the first four states are presented in table 3, for the four cases considered, and figure 4 shows the *binding* energies of the $n = 2$ states, expressed in terms of the effective Rydberg constant versus the mass anisotropy. The degeneracy of the $2s$ and $2p$ states, well-known for the 3D hydrogen atom and remaining for its 2D counterpart [27] is lifted already in the isotropic case, where $E_{2x}^{\text{MoS}_2/\text{h-BN}} = E_{2y}^{\text{MoS}_2/\text{h-BN}} > E_{20}^{\text{MoS}_2/\text{h-BN}}$, in agreement with reference [22]. We notice that the $2s$ energy level is considerably shallower than both $2p$ states for $\Delta\mu = 0$, however, the situation changes as the anisotropy increases and the $2s$ and $2p_y$ states are
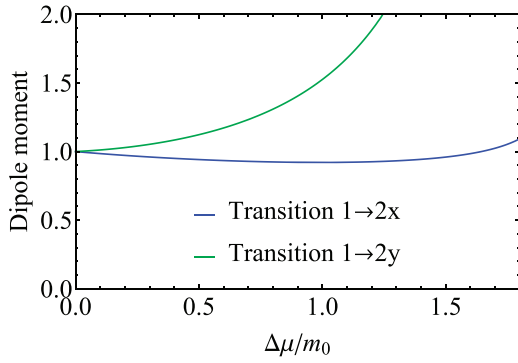
Figure 6. Dipole moment matrix element for the transitions $1s$–$2p_x$ (blue) and $1s$–$2p_y$ (green), plotted against $\Delta\mu$ for a fixed $\bar{\mu}$, normalized to the value for $\Delta\mu = 0$.

inverted. It is also the case of phosphorene (not shown in figure 4) where $\Delta\mu \approx 1.6\bar{\mu}$, $\bar{\mu} \approx 0.55 m_0$. The most stable excited state is the $2p_x$ one (table 3).

Moreover, the inset of figure 4 shows how the dipole moment matrix element for the $|0\rangle \leftrightarrow |2s\rangle$ transition depends on $\Delta\mu$ for a fixed $\bar{\mu}$. This dependence is qualitatively similar to that for the ground state (figure 1). The calculated values are presented in table 4. It is interesting to compare the transition matrix elements from exciton vacuum to the $1s$ and $2s$ states, which ratio, within the effective mass approximation, is determined by $|\Psi_1(0)/\Psi_{20}(0)|^2$. We calculated the values of 3.49 and 4.99 for h-BN/BP/h-BN and h-BN/MoS$_2$/h-BN structures, respectively. The square of this parameter determines the relative strengths of these transitions leading to the exciton creation or recombination.

The electron densities corresponding to the excited states for the h-BN/BP/h-BN and h-BN/MoS$_2$/h-BN structures are shown in figure 5. It is noteworthy how much more extended the $2p$ state are, in comparison with the $2s$ one, in both cases, despite at least one of them corresponds to the largest binding energy. Also we can see the reason why $E_{2x}^{\text{BP/h-BN}} > E_{2y}^{\text{BP/h-BN}}$, the stronger confinement in the x-direction in the former case.

3.4. Dipole transition matrix elements between s and p states

The dipole transitions considered above lead to creation or annihilation of the exciton. Yet, dipole matrix elements between the p and s states determine the rates of 'intraband optical transitions', Stark shift, etc. Within the effective mass approximation, these rates are entirely determined by the envelope functions [40]. Among the states considered here, dipole transitions induced by linear-polarized light are possible between s-type (Ψ_1 and Ψ_{20}) and p-type (Ψ_{2x} and Ψ_{2y}) states, while the reminding matrix elements are equal to zero. Limiting ourselves by considering only the transitions between the ground and excited states, we have:

$$\langle \Psi_1 | x | \Psi_{2x} \rangle = C_1 C_{2x}^* \frac{1}{\sqrt{a_{2x}^3 b_{2x}}}$$

$$\times \int_0^{2\pi} \int_0^\infty \rho_{2x}^3 \cos^2(\theta) \mathrm{e}^{-t(\theta)\rho_{2x}} \, \mathrm{d}\rho_{2x} \, \mathrm{d}\theta,$$

(42)

where

$$t(\theta) = \sqrt{\frac{a_1}{a_{2x}} \cos^2\theta + \frac{b_1}{b_{2x}} \sin^2\theta + 1}$$

(43)

and $C_1 = \sqrt{2/\pi}(a_1 b_1)^{1/4}$. Integrating with respect to ρ_{2x}, we obtain:

$$\langle \Psi_1 | x | \Psi_{2x} \rangle = C_1 C_{2x}^* \frac{1}{\sqrt{a_{2x}^3 b_{2x}}} \int_0^{2\pi} \frac{6 \cos^2(\theta)}{t^4(\theta)} \mathrm{d}\theta.$$

(44)

In a similar way, one obtains

$$\langle \Psi_1 | y | \Psi_{2y} \rangle = C_1 C_{2y}^* \frac{1}{\sqrt{a_{2y} b_{2y}^3}} \int_0^{2\pi} \frac{6 \sin^2(\theta)}{t^4(\theta)} \mathrm{d}\theta.$$

(45)

Figure 6 shows the effect of mass anisotropy on the matrix elements (44) and (45) for $\mu_x + \mu_y = \text{const.}$. We notice the surprising non-monotonic variation of the latter with $\Delta\mu$. Using the appropriate solutions for a_1, b_1, a_{2x}, b_{2x}, a_{2y} and b_{2y}, we obtained $\langle \Psi_1 | x | \Psi_{2x} \rangle = 0.218$ nm and $\langle \Psi_1 | y | \Psi_{2y} \rangle = 0.967$ nm, for the h-BN/BP/h-BN structure.

4. Conclusion

To conclude, we have applied the Rayleigh–Ritz method to the calculation of the ground and lowest excited states' energies in a 2D semiconductor with anisotropic effective masses. In the isotropic limit, these results compare well with previously published data obtained e.g. for monolayer WS$_2$ and MoS$_2$ using other numerical methods, which witnesses the reliability of the variational approach. Moreover, we employed the RK potential with a finite-thickness correction (with a correspondingly renormalized screening parameter), which allowed us to reproduce well the available experimental data [36] on exciton energies in FML films of WS$_2$.

We note that the variational approach is most efficient at low anisotropy, yielding slightly lower binding energies than experiments and other calculations, and this difference grows slightly with increasing anisotropy. We presented calculated the energies of the lowest ($1s$) and $n = 2$ excited states and the dipole transition strengths between them and to the exciton vacuum. For an isotropic system, the most stable of the $n = 2$ excited states is the $2p_x$ one (x denotes the direction in which the effective mass is heavier). The order of the $2s$ and $2p_y$ states depends on the mass anisotropy and also on the dielectric environment of the 2D layer. In particular, the results in table 3 show that it is different for BP encapsulated by h-BN and deposited on a SiO$_2$ substrate. We hope that these findings are of interest for experimentalists and the presented formulae can be useful for computationally inexpensive calculations of the exciton energies and transition matrix elements for other (nearly) 2D materials.

Acknowledgments

Data availability statement

The data that support the findings of this study are available upon reasonable request from the authors.

Appendix A. Extension of the R–K potential to finite L

Equation (8) for the electrostatic potential from the original Rytova's paper [28] reads:

$$\varphi(r) = \frac{\pi q}{\epsilon_2 L} \left[H_0 \left(\frac{2r}{\epsilon L} \right) - Y_0 \left(\frac{2r}{\epsilon L} \right) \right] \equiv \frac{\pi q}{\epsilon_2 L} \mathcal{K}_0 \left(\frac{2r}{\epsilon L} \right),$$
(A.1)

where $\epsilon = \epsilon_2/\epsilon_1$ and ϵ_2 corresponds to the film material. The correspondence between this relation and equation (18) is established by setting $\epsilon_1 \to \kappa$ and

$$\epsilon_2 L = 2r_0, \qquad \epsilon L = \frac{2r_0}{\kappa}.$$
(A.2)

Now we take the Fourier transform (FT) of the potential for a finite thickness L from reference [28], which reads:

$$\varphi(k) = \frac{2\pi q}{\epsilon_2 k} \left[\frac{e^{kL} + \delta}{e^{kL} - \delta} \right],$$
(A.3)

where

$$\delta = \frac{\epsilon - 1}{\epsilon + 1}.$$
(A.4)

For $kL \to 0$ and assuming that ϵ is large (then $1/\epsilon \to 0$), we can apply the following expansions:

$$e^{kL} \simeq 1 + kL + \frac{1}{2}(kL)^2,$$
(A.5)

$$\delta = \frac{1 - 1/\epsilon}{1 + 1/\epsilon} \simeq 1 - 2/\epsilon + 2/\epsilon^2.$$
(A.6)

Therefore, the FT of the potential becomes:

$$\varphi(k) \simeq \frac{2\pi q}{\epsilon_2 k} \left[\frac{1 + kL + 1/2(kL)^2 + 1 - 2/\epsilon + 2/\epsilon^2}{kL + 1/2(kL)^2 + 2/\epsilon - 2/\epsilon^2} \right],$$
(A.7)

or, in our notation,

$$\varphi(k) \simeq \frac{\pi q}{r_0 k} \left[\frac{2}{k + \kappa/r_0} + \frac{1}{2} \frac{L^2 \left(k^2 + \kappa^2/r_0^2 \right)}{(k + \kappa/r_0) \left[1 + \frac{L}{2} \left(k - \kappa/r_0 \right) \right]} \right].$$
(A.8)

The first term corresponds to the potential for $L = 0$, and the second term is the expansion for $L \to 0$. Now to determine the potential in real space one must perform the inverse FT:

$$V(r) = \frac{-q}{(2\pi)^2} \int_0^\infty \int_0^{2\pi} \varphi(k) e^{-ikr \cos \theta} k \, dk \, d\theta,$$
(A.9)

where θ is the angle between $\vec{k}$ and $\vec{r}$. The angular integral yields the Bessel function:

$$V(r) = \frac{-q}{2\pi} \int_0^\infty \varphi(k) J_0(kr) k \, dk.$$
(A.10)

In order to simplify the second term of $\varphi(k)$ we decompose the fraction as follows:

$$\frac{k^2 + \beta^2}{k (k + \beta) (1 + \alpha (k - \beta))} = \frac{A}{k} + \frac{B}{k + \beta} + \frac{C}{1 + \alpha (k - \beta)},$$
(A.11)

where $\alpha \equiv L/2$ and $\beta \equiv \kappa/r_0$. This decomposition yields the coefficients:

$$A = \frac{\beta}{1 - \alpha\beta},$$
(A.12)

$$B = -\frac{2\beta}{1 - 2\alpha\beta},$$
(A.13)

$$C = \frac{1 - 2\alpha\beta + 2\alpha^2\beta^2}{1 - 3\alpha\beta + 2\alpha^2\beta^2}.$$
(A.14)

So, the potential becomes:

$$\begin{aligned}
V(r) &\simeq \frac{-q^2}{r_0} \left\{ \frac{\pi}{2} \mathcal{K}_0 \left(\frac{\kappa r}{r_0} \right) + \alpha^2 \int_0^\infty \left(A + \frac{Bk}{k + \beta} \right. \right. \\
&\left. \left. + \frac{Ck}{1 + \alpha(k - \beta)} \right) J_0(kr) dk \right] \right\} \\
&\simeq \frac{-q^2}{r_0} \left\{ \frac{\pi}{2} \mathcal{K}_0 \left(\frac{\kappa r}{r_0} \right) + \alpha^2 \left[\frac{A}{r} + BF(\beta, r) \right. \right. \\
&\left. \left. + \frac{C}{\alpha} F \left(\frac{1 - \alpha\beta}{\alpha}, r \right) \right] \right\},
\end{aligned}$$
(A.15)

where

$$F(\xi, r) = \int_0^\infty \frac{J_0(kr)}{k + \xi} k \, dk.$$
(A.16)

The first term in (A.15) is the standard RK potential energy (18), while the reminder is the finite-thickness correction. It can be written in the form (19) presented in the main text.

Appendix B. Derivation of equations (28) and (29) for the ground state

From the expression of the ground state energy, equation (26), we obtain the following equations for the parameters a_1 and b_1:

$$\frac{\hbar^2}{4\mu_x} + \frac{q^2}{r_0} \int_0^{2\pi} \int_0^\infty \left(\frac{r\sqrt{a_1 b_1} \cos^2 \theta}{\sqrt{a_1 + (b_1 - a_1) \sin^2 \theta}} - \frac{1}{2} \sqrt{\frac{b_1}{a_1}} \right)$$

$$\times \, \mathcal{K}\left(\frac{\kappa r}{r_0}\right) r \mathrm{e}^{-2\sqrt{a_1+(b_1-a_1)\sin^2\theta}\, r} \, \mathrm{d}r \, \mathrm{d}\theta = 0; \quad \text{(B.1)}$$

$$\frac{\hbar^2}{4\mu_y} + \frac{q^2}{r_0} \int_0^{2\pi} \int_0^\infty \left(\frac{r\sqrt{a_1 b_1}\sin^2\theta}{\sqrt{a_1+(b_1-a_1)\sin^2\theta}} - \frac{1}{2}\sqrt{\frac{a_1}{b_1}}\right)$$

$$\times \, \mathcal{K}\left(\frac{\kappa r}{r_0}\right) r \mathrm{e}^{-2\sqrt{a_1+(b_1-a_1)\sin^2\theta}\, r} \, \mathrm{d}r \, \mathrm{d}\theta = 0. \quad \text{(B.2)}$$

Equations (B.1) and (B.2) can be simplified with the analytically known integrals involving the Struve and Bessel functions [38]:

$$\int_0^\infty \mathrm{e}^{-\alpha x} H_0(\beta x)\mathrm{d}x = \frac{2}{\pi}\frac{\log\left(\frac{\sqrt{\alpha^2+\beta^2}+\beta}{\alpha}\right)}{\sqrt{\alpha^2+\beta^2}}; \quad \text{(B.3)}$$

$$\int_0^\infty \mathrm{e}^{-\alpha x} Y_0\left(\beta x\right)\mathrm{d}x = -\frac{2}{\pi}\frac{1}{\sqrt{\alpha^2+\beta^2}}$$

$$\times \log\left(\frac{\alpha+\sqrt{\alpha^2+\beta^2}}{\beta}\right). \quad \text{(B.4)}$$

The integral

$$I_0(\alpha,\beta) = \int_0^\infty \left[H_0\left(\beta r\right) - Y_0\left(\beta r\right)\right] \mathrm{e}^{-\alpha r}\, \mathrm{d}r$$

$$= \frac{2}{\sqrt{\pi\alpha^2+\beta^2}}\left[\log\left(\frac{\beta+\sqrt{\alpha^2+\beta^2}}{\alpha}\right)\right.$$

$$\left. + \log\left(\frac{\alpha+\sqrt{\alpha^2+\beta^2}}{\beta}\right)\right], \quad \text{(B.5)}$$

and the integral

$$I(\alpha,\beta) = \int_0^\infty \mathcal{K}\left(\beta r\right) r \mathrm{e}^{-\alpha r}\, \mathrm{d}r, \quad \text{(B.6)}$$

can be written as

$$I(\alpha,\beta) = -\frac{\partial}{\partial\alpha} I_0(\alpha,\beta). \quad \text{(B.7)}$$

The ground state energy can be written simply as:

$$E_1 = \frac{\hbar^2}{4}\left(\frac{a_1}{\mu_x} + \frac{b_1}{\mu_y}\right) - \sqrt{a_1 b_1}\frac{q^2}{r_0}\int_0^{2\pi} I(\alpha,\beta)\mathrm{d}\theta, \quad \text{(B.8)}$$

where $\alpha = \sqrt{a_1+(b_1-a_1)\sin^2\theta}$ and $\beta = \kappa/r_0$. Therefore, equations (B.1) and (B.2) read:

$$\frac{\partial E_1}{\partial a_1} = \frac{\hbar^2}{4\mu_x} - \frac{q^2}{2r_0}\frac{b_1}{a_1}\int_0^{2\pi}\left[I(\alpha,\beta) + 4a_1\frac{\cos^2\theta}{\alpha}\frac{\partial I}{\partial\alpha}\right]\mathrm{d}\theta = 0, \quad \text{(B.9)}$$

$$\frac{\partial E_1}{\partial b_1} = \frac{\hbar^2}{4\mu_y} - \frac{q^2}{2r_0}\frac{a_1}{b_1}\int_0^{2\pi}\left[I(\alpha,\beta) + 4b_1\frac{\sin^2\theta}{\alpha}\frac{\partial I}{\partial\alpha}\right]\mathrm{d}\theta = 0. \quad \text{(B.10)}$$

Appendix C. Normalization of the excited states (13)–(15)

Normalization condition for Ψ_{20} reads:

$$|C_{20}|^2 \frac{1}{\sqrt{a_2 b_2}}\int_0^\infty \int_0^{2\pi} \rho_2(1-\rho_2 d)^2 \mathrm{e}^{-2\rho_2}\, \mathrm{d}\rho_2\, \mathrm{d}\theta = 1, \quad \text{(C.1)}$$

$$|C_{20}|^2 \frac{2\pi}{\sqrt{a_2 b_2}}\int_0^\infty \left(\rho_2 - 2\rho_2^2 d + \rho_2^3 d^2\right)\mathrm{e}^{-2\rho_2}\, \mathrm{d}\rho_2 = 1, \quad \text{(C.2)}$$

$$|C_{20}|^2 \frac{2\pi}{\sqrt{a_2 b_2}}\left(\frac{1}{4} - \frac{2}{4}d + \frac{3}{8}d^2\right) = 1, \quad \text{(C.3)}$$

$$|C_{20}|^2 = \frac{4\sqrt{a_2 b_2}}{\pi\left(2 - 4d + 3d^2\right)}. \quad \text{(C.4)}$$

For C_{2x} we have:

$$|C_{2x}|^2 \frac{1}{a_{2x}\sqrt{a_{2x}b_{2x}}}\int_0^\infty \int_0^{2\pi} \rho_2^3 \cos^2(\theta)\mathrm{e}^{-2\rho_2}\, \mathrm{d}\rho_2\, \mathrm{d}\theta = 1, \quad \text{(C.5)}$$

$$|C_{2x}|^2 \frac{3\pi}{8a_{2x}\sqrt{a_{2x}b_{2x}}} = 1, \quad \text{(C.6)}$$

$$|C_{2x}|^2 = \frac{8a_{2x}\sqrt{a_{2x}b_{2x}}}{3\pi}. \quad \text{(C.7)}$$

Similarly, for C_{2y} we obtain:

$$|C_{2y}|^2 = \frac{8b_{2y}\sqrt{a_{2y}b_{2y}}}{3\pi}. \quad \text{(C.8)}$$

Appendix D. Calculation of the trial wave-function parameters for the 2s state

We can write the energy of the 2s state (40) as:

$$\langle\Psi_{20}|\hat{H}|\Psi_{20}\rangle = \frac{\hbar^2}{4}F(a,b,d) - 2\frac{q^2}{r_0}G(a,b,d) \quad \text{(D.1)}$$

with

$$\begin{cases} F(a,b,d) = \left(\frac{a}{\mu_x} + \frac{b}{\mu_y}\right)\frac{2+d^2}{2-4d+3d^2} \\ G(a,b,d) = \frac{1}{(2-4d+3d^2)}\int_0^\infty \int_0^{2\pi} \mathcal{K}\left(\frac{\kappa\rho\sqrt{a^{-1}\cos^2\theta + b^{-1}\sin^2\theta}}{r_0}\right)(1-\rho d)^2\, \rho \mathrm{e}^{-2\rho}\mathrm{d}\rho\, \mathrm{d}\theta. \end{cases} \quad \text{(D.2)}$$

The condition of orthogonality that determines d (17) can be written as:

$$d(a,b) = \frac{f_1(a,b)}{2f_2(a,b)}, \tag{D.3}$$

where

$$f_i(a,b) = \int_0^{\pi/2} t^{-(i+1)}(\theta,a,b)\,\mathrm{d}\theta \tag{D.4}$$

with $t = \sqrt{\frac{a_1}{a}\cos^2\theta + \frac{b_1}{b}\sin^2\theta + 1}$. Therefore,

$$\begin{cases} \partial_a d = \dfrac{f_2 f'_{1a} - f_1 f'_{2a}}{2f_2^2} \\[2mm] \partial_b d = \dfrac{f_2 f'_{1b} - f_1 f'_{2b}}{2f_2^2} \end{cases}, \tag{D.5}$$

and

$$\begin{cases} f'_{ia} = -\dfrac{(i+1)a_1}{2a^2}\displaystyle\int_0^{\pi/2} t^{-(i+2)}(\theta,a,b)\dfrac{\cos^2\theta}{t(\theta,a,b)-1}\mathrm{d}\theta \\[3mm] f'_{ib} = -\dfrac{(i+1)b_1}{2b^2}\displaystyle\int_0^{\pi/2} t^{-(i+2)}(\theta,a,b)\dfrac{\sin^2\theta}{t(\theta,a,b)-1}\mathrm{d}\theta \end{cases}. \tag{D.6}$$

Taking now (D.1), minimization of the energy requires:

$$\begin{cases} \partial_a E_{20}(a,b,d(a,b)) = 0 \\[2mm] \partial_b E_{20}(a,b,d(a,b)) = 0 \end{cases}, \tag{D.7}$$

$$\begin{cases} \dfrac{\hbar^2}{4}\partial_a F(a,b,d(a,b)) - 2\dfrac{q^2}{r_0}\partial_a G(a,b,d(a,b)) = 0 \\[3mm] \dfrac{\hbar^2}{4}\partial_b F(a,b,d(a,b)) - 2\dfrac{q^2}{r_0}\partial_b G(a,b,d(a,b)) = 0 \end{cases}, \tag{D.8}$$

where

$$\partial_a F(a,b,d(a,b)) = \frac{2+d^2}{2-4d+3d^2}\frac{1}{\mu_x} \\ + \left[\frac{a}{\mu_x} + \frac{b}{\mu_y}\right]\left[\frac{8-8d-4d^2}{(3d^2-4d+2)^2}\right]\partial_a d; \tag{D.9}$$

$$\partial_b F(a,b,d(a,b)) = \frac{2+d^2}{2-4d+3d^2}\frac{1}{\mu_y} \\ + \left[\frac{a}{\mu_x} + \frac{b}{\mu_y}\right]\left[\frac{8-8d-4d^2}{(3d^2-4d+2)^2}\right]\partial_b d; \tag{D.10}$$

$$\partial_a G(a,b,d(a,b)) = -\frac{1}{2-4d+3d^2}\int_0^\infty\int_0^{2\pi} \\ \times \frac{\kappa\rho^2}{r_0}\frac{\cos^2\theta}{2a^2\sqrt{a^{-1}\cos^2\theta + b^{-1}\sin^2\theta}}K'_0 \\ \times \left(\frac{\kappa\rho\sqrt{a^{-1}\cos^2\theta + b^{-1}\sin^2\theta}}{r_0}\right) \\ \times (1-\rho d)^2\mathrm{e}^{-2\rho}\,\mathrm{d}\rho\,\mathrm{d}\theta$$

$$+\ \partial_a d(a,b) \times \left[\frac{6d-4}{2-4d+3d^2}\right. \\ -\ G(a,b,d(a,b))\frac{1}{2-4d+3d^2}\int_0^\infty\int_0^{2\pi} \\ \times\ \mathcal{K}\left(\frac{\kappa\rho\sqrt{a^{-1}\cos^2\theta + b^{-1}\sin^2\theta}}{r_0}\right) \\ \left.\times\ (1-\rho d)\rho^2\mathrm{e}^{-2\rho}\right]; \tag{D.11}$$

$$\partial_b G(a,b,d(a,b)) = -\frac{1}{2-4d+3d^2}\int_0^\infty\int_0^{2\pi} \\ \times\ \frac{\kappa\rho^2}{r_0}\frac{\sin^2\theta}{2b^2\sqrt{a^{-1}\cos^2\theta + b^{-1}\sin^2\theta}} \\ \times\ K'_0\left(\frac{\kappa\rho\sqrt{a^{-1}\cos^2\theta + b^{-1}\sin^2\theta}}{r_0}\right) \\ \times\ (1-\rho d)^2\mathrm{e}^{-2\rho}\,\mathrm{d}\rho\,\mathrm{d}\theta + \partial_b d(a,b) \\ \times\ \left[\frac{6d-4}{2-4d+3d^2}G(a,b,d(a,b))\right. \\ -\ \frac{1}{2-4d+3d^2}\int_0^\infty\int_0^{2\pi} \\ \times\ \mathcal{K}\left(\frac{\kappa\rho\sqrt{a^{-1}\cos^2\theta + b^{-1}\sin^2\theta}}{r_0}\right) \\ \left.\times\ (1-\rho d)\rho^2\mathrm{e}^{-2\rho}\right]. \tag{D.12}$$

The equations $\partial_a G(a,b,d(a,b)) = \partial_b G(a,b,d(a,b)) = 0$ are solved numerically.

ORCID iDs

Carlos Trallero-Giner ⓘ https://orcid.org/0000-0002-1640-8591

Mikhail I Vasilevskiy ⓘ https://orcid.org/0000-0003-2930-9434

References

[1] Novoselov K S, Geim A K, Morozov S V, Jiang D, Zhang Y, Dubonos S V, Grigorieva I V and Firsov A A 2004 *Science* **306** 666–9

[2] Khan K, Tareen A K, Aslam M, Wang R, Zhang Y, Mahmood A, Ouyang Z, Zhang H and Guo Z 2020 *J. Mater. Chem.* C **8** 387–440

[3] Geim A K and Grigorieva I V 2013 *Nature* **499** 419

[4] Ferrari A C *et al* 2015 *Nanoscale* **7** 4598–810

[5] Olsen T, Latini S, Rasmussen F and Thygesen K S 2016 *Phys. Rev. Lett.* **116** 056401

[6] Wang G, Chernikov A, Glazov M M, Heinz T F, Marie X, Amand T and Urbaszek B 2018 *Rev. Mod. Phys.* **90** 021001

[7] Carvalho A, Wang M, Zhu X, Rodin A S, Su H and Castro Neto A H 2016 *Nat. Rev. Mater.* **1** 16061

[8] Cho K, Yang J and Lu Y 2017 *J. Mater. Res.* **32** 2839
[9] Ferreira F and Ribeiro R M 2017 *Phys. Rev. B* **96** 115431
[10] Castellanos-Gomez A *et al* 2014 *2D Mater.* **1** 25001
[11] Tran V, Fei R and Yang L 2015 *2D Mater.* **2** 044014
[12] Castellanos-Gomez A 2015 *J. Phys. Chem. Lett.* **6** 4280
[13] Ryzhii V, Otsuji T, Ryzhii M, Dubinov A A, Aleshkin V Y, Karasik V E and Shur M S 2019 *Phys. Rev. B* **100** 115436
[14] Lu S B, Miao L L, Guo Z N, Qi X, Zhao C J, Zhang H, Wen S C, Tang D Y and Fan D Y 2015 *Opt. Express* **23** 11183–94
[15] Rodrigues M J L F, de Matos C J S, Ho Y W, Peixoto H, de Oliveira R E P, Wu H-Y, Neto A H C and Viana-Gomes J 2016 *Adv. Mater.* **28** 10693–700
[16] Hipolito F and Pedersen T G 2018 *Phys. Rev. B* **97** 035431
[17] Zhang G, Chaves A, Huang S, Wang F, Xing Q, Low T and Yan H 2018 *Sci. Adv.* **4** eaap9977
[18] Li P and Appelbaum I 2014 *Phys. Rev. B* **90** 115439
[19] Cong C, Shang J, Wang Y and Yu T 2017 *Adv. Opt. Mater.* **6** 1700767
[20] Arra S, Babar R and Kabir M 2019 *Phys. Rev. B* **99** 045432
[21] Rudenko A N and Katsnelson M I 2014 *Phys. Rev. B* **89** 201408(R)
[22] Chaves A, Low T, Avouris P, Çakır D and Peeters F M 2015 *Phys. Rev. B* **91** 155311
[23] Henriques J C G and Peres N M R 2020 *Phys. Rev. B* **101** 35406
[24] Ritz W 1909 *J. für die Reine Angewandte Math.* **1909** 1–61
[25] Hanamura E, Nagaosa N, Kumagai M and Takagahara T 1988 *Mater. Sci. Eng. B* **1** 255–8
[26] Martins Quintela M F C and Peres N M R 2020 *Eur. Phys. J. B* **93** 222

[27] Yang X L, Guo S H, Chan F T, Wong K W and Ching W Y 1991 *Phys. Rev. A* **43** 1186–96
[28] Rytova N S 1967 *Moscow Univ. Phys. Bull.* **3** 18
[29] Keldysh L V 1979 *JETP Lett.* **29** 658
[30] Abramowitz M and Stegun I A (ed) 1972 *Handbook of Mathematical Functions* (New York: Dover)
[31] Vasilevskiy M I, Santiago-Pérez D G, Trallero-Giner C, Peres N M R and Kavokin A 2015 *Phys. Rev. B* **92** 245435
[32] Gomes J N S, Trallero-Giner C, Peres N M R and Vasilevskiy M I 2020 *J. Appl. Phys.* **127** 133101
[33] Cudazzo P, Tokatly I V and Rubio A 2011 *Phys. Rev. B* **84** 085406
[34] Sohier T, Gibertini M, Calandra M, Mauri F and Marzari N 2017 *Nano Lett.* **17** 3758–63
[35] Chate P A, Sathe D J and Hankare P P 2013 *Appl. Nanosci.* **3** 19–23
[36] Chernikov A, Berkelbach T C, Hill H M, Rigosi A, Li Y, Aslan O B, Reichman D R, Hybertsen M S and Heinz T F 2014 *Phys. Rev. Lett.* **113** 076802
[37] Sohier T, Calandra M and Mauri F 2016 *Phys. Rev. B* **94** 085415
[38] Gradshteyn I S and Ryzhik I M 2014 *Table of Integrals, Series, and Products* (New York: Academic)
[39] Goryca M *et al* 2019 *Nat. Commun.* **10** 1–12
[40] Basu P K 1997 *Theory of Optical Processes in Semiconductors* (Oxford: Clarendon)
[41] Faria Junior P E, Kurpas M, Gmitra M and Fabian J 2019 *Phys. Rev. B* **100** 115203